Research Article

Preparation of Ag@AgCl/GO Material with Efficient Visible-Light Photocatalytic Performance

Daxiang Gao [ID],[1] **Zhen Shu,**[2] **and Xiaozhong Huang**[1]

[1]*Jiangsu Vocational College of Agriculture and Forestry, Jiangsu, Jurong 212400, China*
[2]*Anhui Xuchen Biotechnology Co. Ltd, Anhui, BengBu 233000, China*

Correspondence should be addressed to Daxiang Gao; gaodaxiang@jsafc.edu.cn

Ag@AgCl/GO was prepared by chemical coupling, in-situ deposition of supported AgCl, and photoreduction. The morphology, structure, and surface area of the prepared Ag@AgCl/GO were characterized by SEM, TEM, FT-IR, Raman spectra, and BET. The optical properties of the photocatalyst were analyzed by PL and UV-Vis DRS, respectively. The surface electrical properties and degradation stability were evaluated by zeta potential measurement and cyclic catalytic degradation experiments, and the photocatalytic mechanism was proposed in detail based on the ESR test and trapping experiment. The results showed that Ag@AgCl nanoparticles were spherical and cluster distributed on the folded structure of GO. The prepared Ag@AgCl/GO had good adsorption performance and photocatalytic degradation stability. The material showed good visible light catalytic performance; especially, the degradation rates of cationic dyes RhB and MB were significantly higher than those of anionic dyes MO and CR, and their degradation processes were in line with the quasi-first-order reaction kinetics. Holes (h^+) and superoxide radicals ($\cdot O_2$ -) were the main active species for the degradation of RhB.

1. Introduction

Wang et al. [1] first discovered the excellent visible light degradation performance of Ag@AgCl for methyl orange. In recent years, Ag@AgCl plasma photocatalyst has attracted extensive attention [2–4]. Ag@AgCl refers to the simple state of Ag^0 decomposed by AgCl under light conditions, which is loaded on the surface of AgCl. Therefore, Ag@AgCl photocatalyst is a new visible photocatalytic material based on the nanometal surface plasma effect and semiconductor photocatalysis effect. The surface plasma resonance (SPR) effect is an important reason for the good performance of silver halide photocatalyst [5]. Although Ag@AgCl has good photocatalytic activity, AgCl has poor photochemical stability, easy agglomeration, and high recombination rate of photogenerated electrons and holes [6]. Therefore, its application in photocatalytic research is limited. Through the construction of AgCl and g-C_3N_4 [7, 8], AgBr [9], V_2O_5 [10], $B_4Ti_3O_{12}$ [11], WO_3 [12], MIL-88A [13], and polyaniline [14]

composite photocatalysts, the problem of easy agglomeration of AgCl nanoparticles is solved, and the photocorrosivity of the material is reduced, so as to improve its photochemical stability and photocatalytic activity [15].

Graphene oxide (GO) is a novel carbon-based material, which is a derivative of graphene. It is a monolayer graphene sheet composed of carboxyl, hydroxyl, epoxy, and other oxygen-containing functional groups. The surface of GO is wrinkled, with excellent hydrophilicity, large specific surface area, and low toxicity. The composites formed with photocatalysts have attracted great attention in the fields of photocatalysis, such as GO and TiO_2 [16, 17], Ag_3PO_4 [18, 19], BiOI [20], $BiVO_4$ [21], and $Zn(OH)_2$ [22]. At present, in the research of GO and AgCl composite photocatalyst materials, Wang Shuang et al. successfully prepared AgCl/GO composite visible light catalyst by microemulsion method. The degradation rate of methyl orange (MO) reached more than 91% after 100 min visible light irradiation [23]. Chao Xu et al. successfully prepared

graphene oxide-supported uniform Ag@AgCl core-shell nanoparticle composites by a facile two-step synthetic process, and these nanoparticle composites display effective photodegradation of methylene orange dye under visible light irradiation, which indicates their potential applications in environmental areas [24].

This study aims at the problems of poor photochemical stability, easy agglomeration, insufficient adsorption capacity, and difficult recycling of AgCl. By introducing GO and using the property of sodium alginate (SA) aqueous solution and divalent cation (such as Ca^{2+}) to form a stable gel, AgCl was successfully loaded on GO by chemical coupling and in-situ deposition, and Ag@AgCl/GO was prepared by photoinduced reduction. The photocatalytic material can be used for the degradation of actual organic pollution wastewater with the advantages of strong adsorption capacity, short photocatalytic degradation time, high catalytic efficiency, wide visible light response range, and easy recycling.

2. Materials and Methods

2.1. Preparation of Photocatalytic Materials

2.1.1. Preparation of GO.
First, 92 mL concentrated sulfuric acid was cooled to 0°C in an ice bath, and 2 g flake graphite and 2 g $NaNO_3$ were added to the concentrated sulfuric acid under magnetic stirring. Then, 12 g $KMnO_4$ was slowly put into the above-mixed solution, and the reaction system was kept below 5°C for 2 h, heated up to 40°C for 2 h, diluted with 60 mL deionized water, and stirred for 1 h. Finally, 15 mL 30% H_2O_2 solution was used to remove unreacted $KMnO_4$. After standing overnight, GO was obtained by ultrasonic, centrifugation, and washing to neutralize with deionized water in succession, and the prepared sample was dried at 60°C for 2 h.

2.1.2. Preparation of Ag@AgCl/GO.
Preparation principle: in the first step, when GO dispersion is mixed with the mixed solution of sodium alginate (SA) and cetyl-trimethylammonium bromide (CTAB), alginate ions will be adsorbed on the GO layer due to the action of hydrogen bond and the surfactant of CTAB. In the second step, after adding silver nitrate, due to the electrostatic attraction, the positively charged silver ion (Ag^+) will attract the negatively charged alginate ion and the carboxylate group (–COO–) on GO, so that the silver ion is closely surrounded in GO.

Specific preparation method: 3 mL 4 g/L SA solution was added to 60 mL 1 g/L GO dispersion solution, stirred, and ultrasound for 15 min to mix fully. 1.5 mL 10 g/L CTAB surfactant was put into the mixture and dispersed by ultrasonic for 30 min. Under magnetic stirring, 9 mL 50 g/L $AgNO_3$ solution was slowly dropped into the mixture. After continued stirring for 15 min, 9 mL 20 g/L $CaCl_2$ solution was slowly added to the above-mixed system to form insoluble particles by using the crosslinking effect of Ca^{2+} and AgCl precipitation. It is allowed to stand for 24 h after magnetic stirring for 30 min. The particle precipitate was obtained by filtering through double-layer gauze and washed

with deionized water for 5 times. The filtrate was retained. Then, the precipitate was added to a 250 mL flask containing 50 mL deionized water and irradiated for 1 h by using a 350 W xenon lamp under magnetic stirring. Ag@AgCl/GO (denoted as GO+) was obtained through double-layer gauze filtration and vacuum freeze-dried. Meanwhile, the above-mentioned filtrate was centrifuged, and the obtained Ag@AgCl precipitate was treated according to the same method.

2.2. Characterizations of Photocatalytic Materials.
The morphologies were collected with a field emission scanning electron microscope (SEM) (Quattro S, FEI, USA). The microstructures were examined by a transmission electron microscope (TEM) (JEM-2100, Japan Electronics Co., Ltd). The chemical bonding status of the samples was analyzed on an FT-IR spectrometer (IRtracer-100, Shimadzu, Japan), with a resolution of $4 cm^{-1}$ and a scanning range of $400–4000 cm^{-1}$. The Raman spectra of the samples were measured with a laser confocal Raman spectrometer (Lab-RAM HR Evolution, HORIBA, France). The specific surface area of the samples was calculated by using an automatic-specific surface area analyzer (BELSORP-max, Micro-tracBEL, Japan). The zeta potential of the samples was measured by a zeta potentiometer (ZEN3600, Malvern, UK). The UV-visible absorbance spectra of the samples were obtained by means of a UV-visible spectrophotometer (lambda750, PerkinElmer, America). The photo-luminescence (PL) spectra were measured under 315 nm excitation wavelength by a fluorescence spectrophotometer (FluoroMax-4, Horiba, France). UV-visible absorbance spectra of the degradation solution were obtained by means of a UV-visible spectrophotometer (UV-2600, Shimadzu, Japan). The electron spin resonance (ESR) spectra in the solution were detected under dark or visible light ($\lambda > 420 nm$) with an electron paramagnetic resonance spectrometer (JES-FA200, Japan Electronics Co., Ltd).

2.3. Photocatalytic Test

2.3.1. Degradation Dynamics Analyses.
In order to study the kinetic relationship of photocatalytic degradation of pollutants by the prepared GO+, the Langmuir–Hinshelwood model was used to obtain the first-order photocatalytic reaction rate equation: $\ln (C_0/C_t) = kt + A$, where k is the apparent rate constant (min^{-1}), and C_0 and C_t are the pollutant concentration (mg/L) at reaction time 0 and t, respectively.

2.3.2. Photocatalytic Activity Analyses.
0.2 g of the prepared GO+ was added into a 100 mL triangular flask, and then, 60 mL 10 mg/L RhB (or another dye) solution was added. After mixing, the initial pH value was adjusted to 6.5, and the temperature was controlled at 40°C. After magnetic stirring for 30 min in dark, the triangular flask was placed under a 300 W xenon lamp ($\lambda > 420 nm$), and the distance between the light source and the liquid level was about 5 cm. The time was started under magnetic stirring, and 3 mL of the upper

reaction solution was taken out every 2 min as the test solution. The absorbance change was measured to evaluate the degradation activity of the catalytic material. The relationship curve between the C_t/C_0 of the dye solution and the degradation time t in the degradation process is the photodegradation curve, where C_0 and C_t are the dye concentration (mg/L) at reaction times 0 and t, respectively.

3. Results and Discussion

3.1. Morphology and Elemental Composition. Figures 1 and 2 show the SEM image and TEM image of the GO + composites, respectively. The folded structure of the catalytic material is loaded with a large number of irregular AgCl and Ag@AgCl nanoparticles, which are overlapped and stacked in clusters. AgCl particles are spherical, with uneven particle size of 50 ~ 100 nm. It can be seen that Ag@AgCl particles are successfully loaded on Ca^{2+} cross-linked GO/SA folds. The fold structure can act as a partition to effectively divide the clustered Ag@AgCl particles, which is conducive to the adsorption and rapid degradation of dyes by the composite to a certain extent, and effectively improve the photocatalytic performance of the composite. From the electron diffraction pattern of the composite (Figure 3), it can be seen that the catalytic material shows an obvious polycrystalline diffraction ring.

Figures 4 and 5 show the EDS spectra and the surface scan distribution of the main elements of the GO + composites, respectively. The sample contains Ag, Cl, C, O, N, Ca, Br, and other elements. The mass concentration of Ag element was higher than that of C element, and the concentration of Ag atom was also higher than that of C and O, while the content of silver atom is about four times that of chlorine atom, namely, Ag: AgCl = 4 : 1, indicating that each AgCl particle surface was roughly adhered by Ag nanoparticles (AgNPs). In addition, the composites also contain a small amount of AgBr particles and CTAB cations, and a small amount of AgBr particles can also cooperate with Ag@AgCl for the catalytic degradation of pollutants.

3.2. FT-IR Analysis. For the GO and SA, the absorption peaks of GO at 1040 and 1220 cm^{-1} (Figure 6) derive from the C–O and C–OH, respectively. At 1415, 1622, and 1730 cm^{-1}, respectively, there are vibration absorption peaks of carboxyl C–O, "benzene ring" $C=C$, and carboxyl $C=O$ [25]. The characteristic peaks of hydroxyl (-OH) appear at 3370 cm^{-1} (GO) and 3320 cm^{-1} (SA). The absorption peaks of SA at 1596 cm^{-1} and 1405 cm^{-1} belong to the antisymmetric and symmetrical stretching vibration of –COO–, respectively, and the absorption peak at 1028 cm^{-1} is attributed to the C–O–C.

For the GO+, the characteristic peak of AgCl appears at 610 cm^{-1} of the fingerprint area [23], and the absorption peak at 1040 cm^{-1} is attributed to the vibration of the C–O–C. Compared with pure GO, the peak intensity of the C–O–C is significantly weakened. The peak at 1411 cm^{-1} may be caused by the C–O vibration of the –COO– groups.
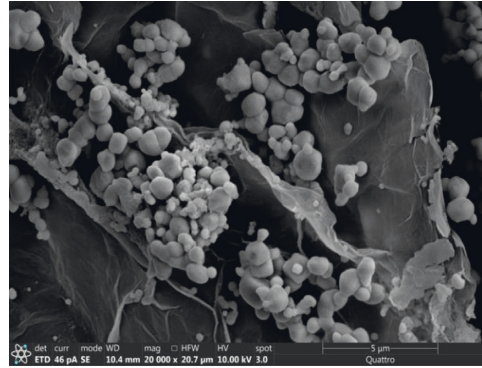

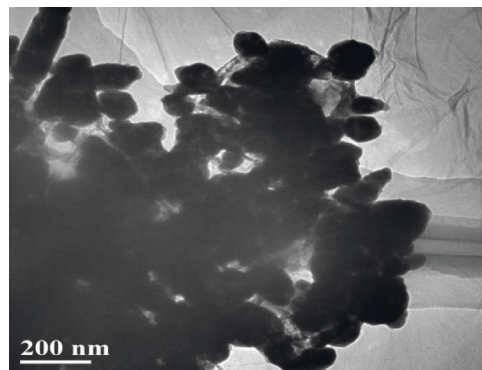FIGURE 1: The SEM of the sample (SEM).
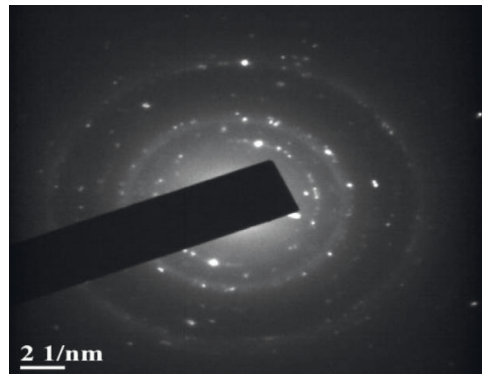

FIGURE 2: The TEM of the sample (TEM).

FIGURE 3: Electron diffraction pattern of the sample.

The peak at 1609 cm^{-1} is mainly attributed to the deformation vibration of adsorbed water molecules (bending vibration peak of water molecules). The stretching vibration peaks of C–OH and carboxyl $C=O$ at 1220 cm^{-1} and 1730 cm^{-1} (GO) disappeared in the GO+. The absorption peaks at 2925 cm^{-1} and 2850 cm^{-1} are the manifestation of symmetric and asymmetric stretching vibrations of methylene ($-CH_2-$) of CTAB [26]. It is known that the vibration peak of free hydroxyl is located in 3640 ~ 3610 cm^{-1}, while the stretching vibration peak of associated hydroxyl exists in 3400 ~ 3200 cm^{-1}. The wide absorption band at 3380 cm^{-1} is
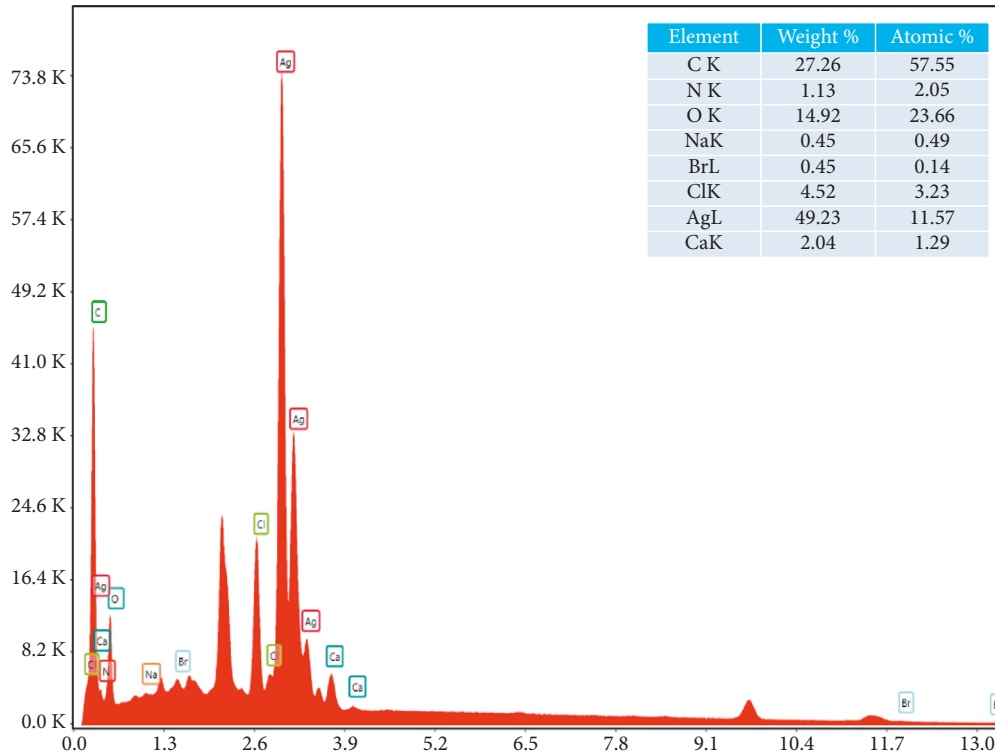
Element	Weight %	Atomic %
C K	27.26	57.55
N K	1.13	2.05
O K	14.92	23.66
NaK	0.45	0.49
BrL	0.45	0.14
ClK	4.52	3.23
AgL	49.23	11.57
CaK	2.04	1.29

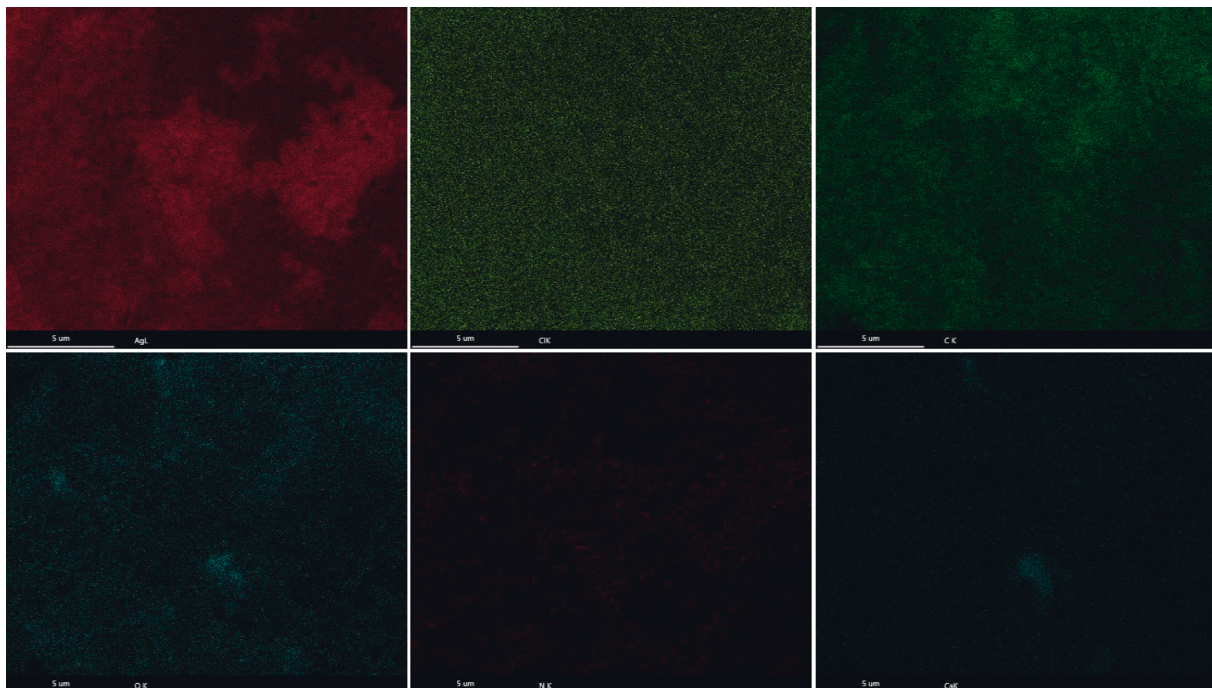FIGURE 4: The EDS profiles of the sample.

FIGURE 5: Elemental analysis of the sample.

attributed to the stretching vibration of the O–H bond of the oxygen-containing functional group [27]. Compared with pure GO, the intensity of the characteristic peak is significantly reduced, indicating that the –OH content in the GO+ is greatly reduced compared with GO and SA. This is because most –OH groups participate in the crosslinking reaction, resulting in the reduction of intramolecular hydrogen bonds and intermolecular hydrogen bonds. Therefore, the infrared band of the –OH peak is widened and slightly red-shifted [28].
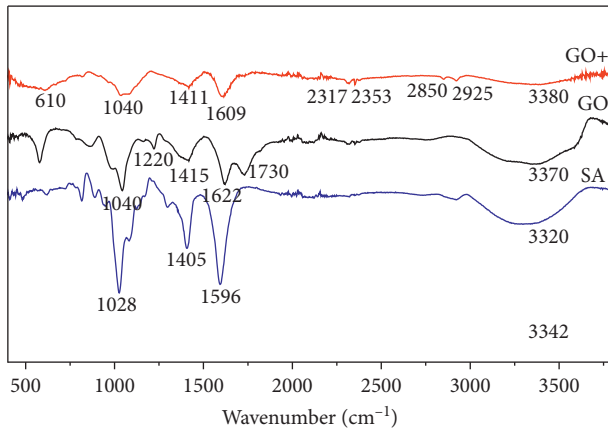
FIGURE 6: FT-IR spectra of the GO+, GO, and SA.

FIGURE 7: Raman spectra of the GO+ and GO.

The characteristic peak of the oxygen-containing functional groups on the surface of the GO+ is significantly reduced, and the intensity of the characteristic peak is significantly weakened at $1500 \sim 1750 \, cm^{-1}$, indicating that a stable coordination crosslinking is formed between the oxygen-containing groups on the surface of GO and the divalent cations (Ca^{2+}), and some oxygen-containing functions are lost in the process of crosslinking and recombination [23].

3.3. Raman Spectra Analysis.
The D peak in Raman spectra represents the edge defect and amorphous structure of graphene, and the G peak means the ordered SP2 bond structure [29]. Figure 7 shows the Raman spectra of the GO+ and pure GO. The GO + has two characteristic peaks of GO at $1350 \, cm^{-1}$ (D peak) and $1581 \, cm^{-1}$ (G peak) [30], indicating that the GO + has the composition and structure of GO. The weakening of the two characteristic peaks of the GO+ is due to the strong interaction between GO and AgCl and the crosslinking with Ca^{2+}. The integral intensity ratio (I_D/I_G) of D peak and G peak increased from 0.90 to 0.93, which is due to the increase in structural defects and disorders caused by crosslinking reaction and the loss of some oxygen-containing functional groups [31].

3.4. Adsorption Property Analysis.
Generally, the larger the specific surface area of the material is, the stronger the adsorption performance of the material is [32]. The BET-specific surface area can be calculated from the N_2 adsorption-desorption isotherm of the GO+. Taking the sample prepared with equal mass SA instead of GO (denoted as SA+) as the control, Figure 8 shows that the isotherm of the GO + conforms to the class IV isotherm, indicating that the composite has mesoporous structure, which is conducive to the absorption of visible light and reduces the recombination of e^- and h^+ [33]. The adsorption hysteresis loop of the GO+ is not obvious compared with SA+, indicating that the GO + has no significant capillary condensation in the hole, and the adsorption performance is relatively strong. The specific surface area and average pore size of the material are $1.2645 \, m^2/g$ and $18.021 \, nm$, respectively, and the pore

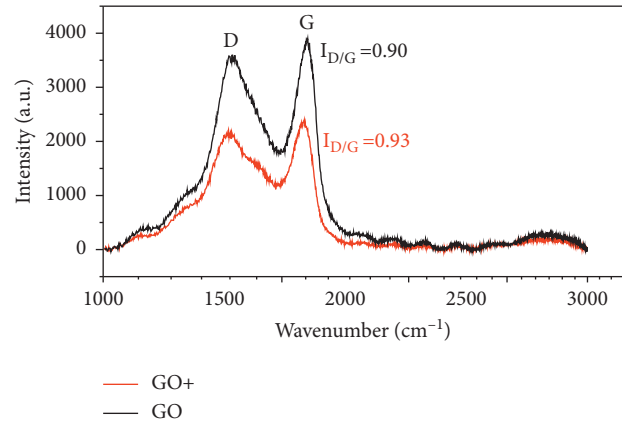size distribution is between 2 and 100 nm. According to the photocatalytic oxidation mechanism, the recombination of photogenerated electrons and holes on the catalyst surface is completed within $10^{-9} \, s$, but the carrier capture rate is relatively slow, which usually takes $10^{-8} \sim 10^{-7} \, s$. Therefore, only the pollutants adsorbed on the catalyst surface are likely to obtain highly active electrons and holes for reaction. Because GO has a large specific surface area and strong adsorption capacity of carbon-based materials, dispersing and depositing Ag@AgCl on GO can effectively enhance the adsorption performance of the GO + to pollutants and the ability of the photocatalytic degradation of pollutants.

3.5. Fluorescence Property.
PL spectroscopy is an effective method to study the recombination efficiency of photogenerated carriers. The fluorescence intensity reflects the recombination efficiency of electron-hole pairs. Generally, the lower the intensity of PL, the lower the recombination rate of photogenerated electrons and holes. Figure 9 shows the PL spectra of the prepared GO+ and Ag@AgCl. Both samples had fluorescence peaks at 430 nm, but the intensity of the emission peak of the GO+ was much weaker than that of Ag@ AgCl, indicating that the probability of photogenerated charge recombination of the GO+ is low. Thus, the addition of the GO can reduce the recombination of photogenerated electrons and holes to enhance the photocatalytic activity.

3.6. UV-Vis DRS Characterization.
It is reported that the indirect energy band gap of AgCl is about 3.25 eV. Except for the absorption band in the UV region, AgCl has almost no absorption performance in $400 \sim 800 \, nm$ [34]. Therefore, the strong absorption performance of Ag@AgCl in the visible light region should be the resonance absorption band generated by the SPR effect of Ag nanoparticles [35]. It can be seen from Figure 10 that the GO + still has strong absorption in the UV-vis region, and the absorption in the visible light region is still in a wide wavelength range. It indicated that GO played a synergistic effect on the visible light absorption of Ag@AgCl to some extent.
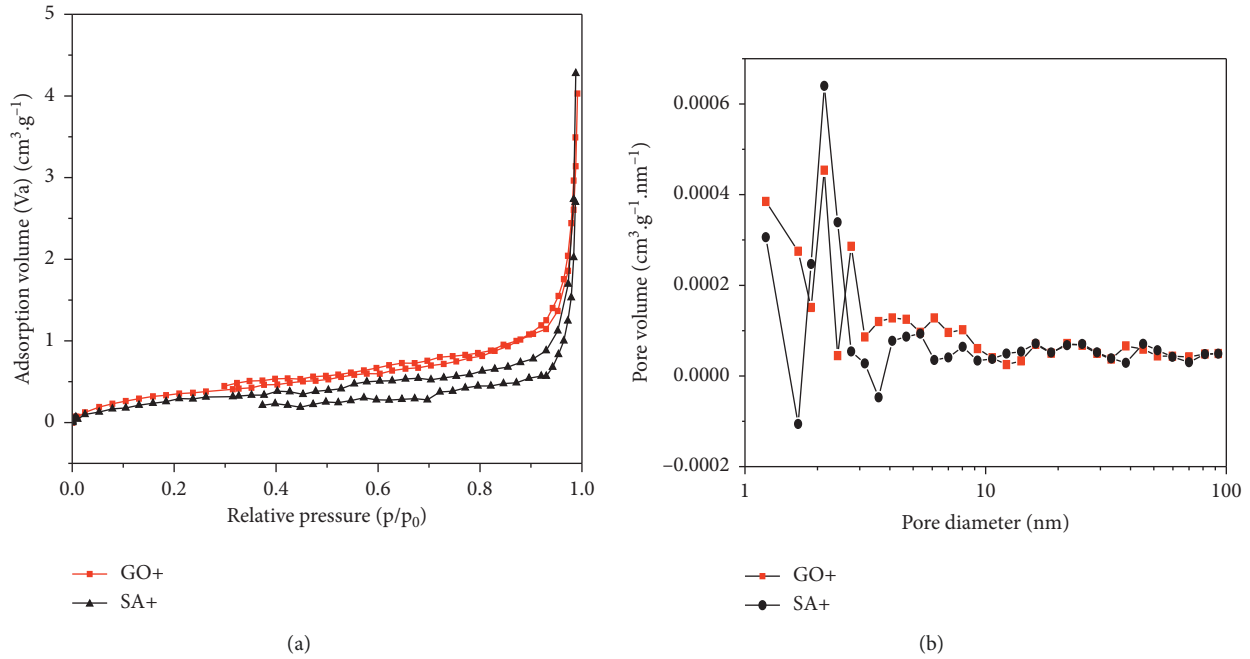
(a)

(b)

FIGURE 8: (a) Adsortion-desorption isotherms and (b) pore size distribution of GO+ and SA+.
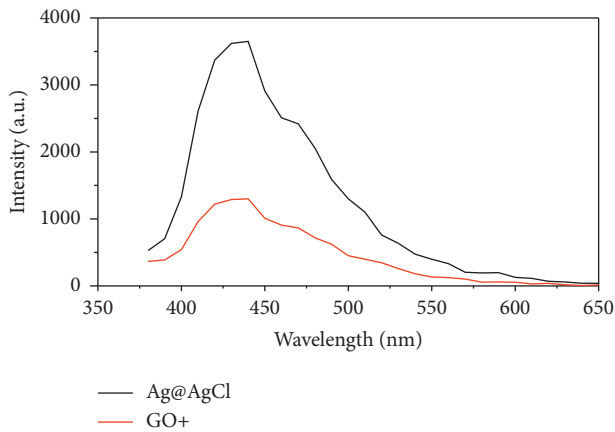

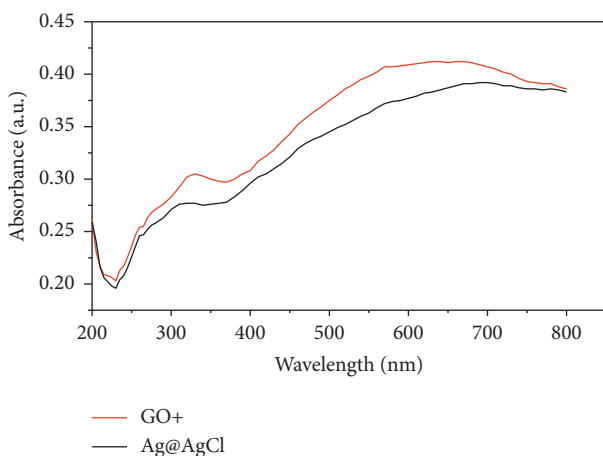FIGURE 9: Photoluminescence (PL) spectra of the GO+ and Ag@AgCl.

FIGURE 10: UV-vis DRS of the GO+ and Ag@AgCl.

3.7. Photocatalytic Degradation Performance.

Figure 11 shows the degradation curves of rhodamine (RhB), methylene blue (MB), methyl orange (MO), and carmine red (CR) by the GO + under visible light irradiation. The characteristic absorption of RhB at 554 nm in the visible region ($n \longrightarrow \pi^*$ electron transition on $C=O$, $C=N$) and 270 nm in the UV region ($\pi \longrightarrow \pi^*$ electron transition on benzene ring) decreased rapidly with the extension of reaction time, indicating that the main structural substances of RhB were completely decomposed. MB has characteristic absorption peaks at 664, 609, 291.8, and 246.4 nm, of which 664 nm and 291 nm correspond to the absorption peaks produced by the super-conjugated structure and the $\pi \longrightarrow \pi^*$ transition of benzene ring, respectively. These characteristic absorption peaks disappeared after the reaction, indicating that MB had been degraded after the reaction. The characteristic peaks of MO at 465.2, 271.6 nm were produced by the –N = N-azo and benzene ring conjugate system, respectively. After 12 min, there were no obvious absorption peaks in the UV-vis region, indicating that MO was completely catalytic degraded. The typical absorption peaks of CR appeared at 514.5 nm and 280 nm. After 12 min, the structure at 514.5 nm was effectively degraded, but the characteristic peaks at 280 nm were still obvious, indicating that the characteristic groups still existed.

Figure 12 shows that the photocatalytic degradation of the four dyes all follows the quasi-first-order kinetics reaction. The degradation rate constants (k) of RhB and MB are 0.5381 min^{-1} and 0.4989 min^{-1} respectively, which are higher than those of anionic dyes MO (0.2573 min^{-1}) and CR (0.2573 min^{-1}). The results showed that the GO + has a stronger ability to degrade cationic dyes RhB and MB, a weaker ability to degrade anionic dye MO, and the worst
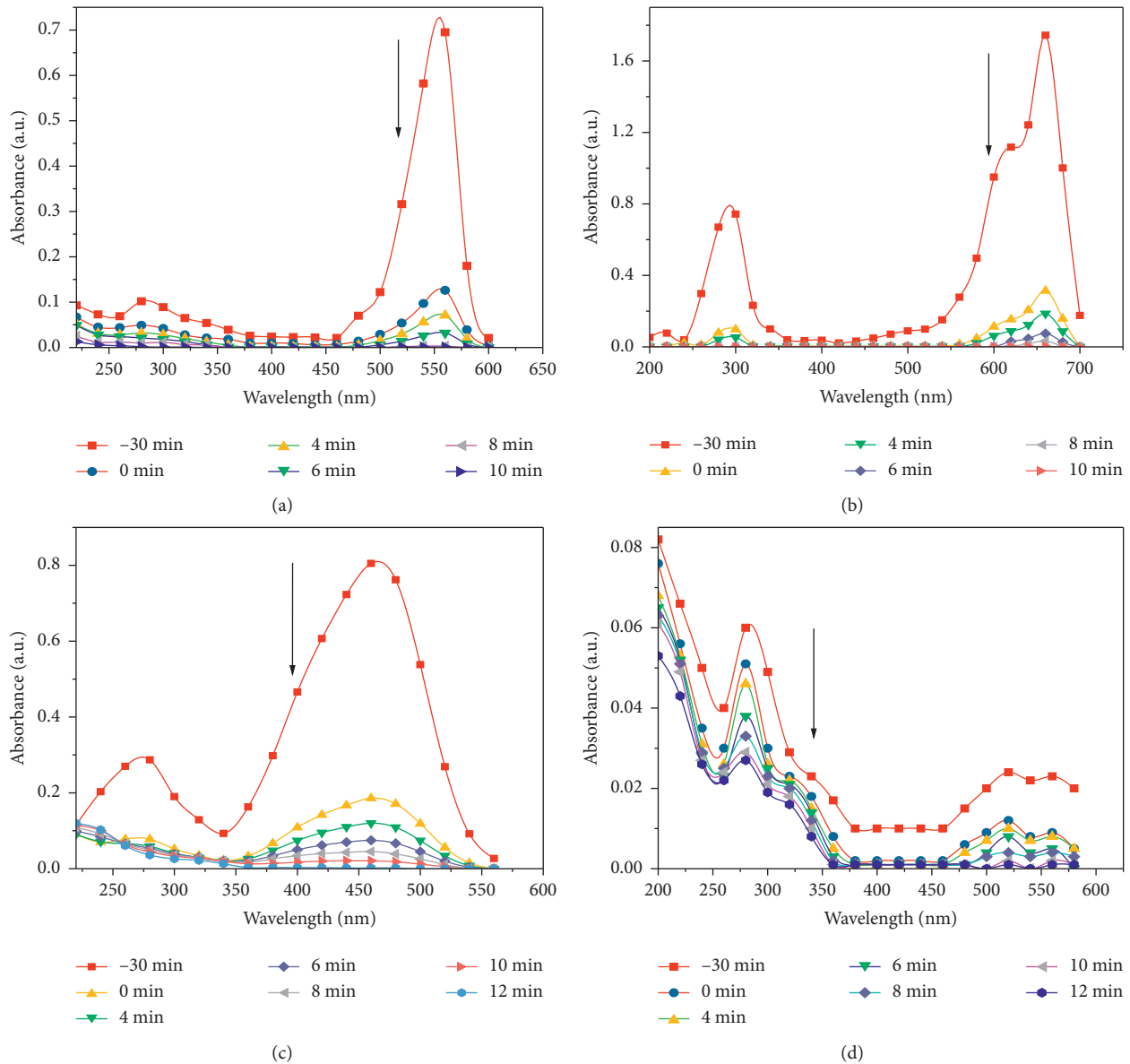
FIGURE 11: Absorption spectra of visible light irradiation by the GO+: RhB (a), MB (b), MO (c), CR (d).

ability to degrade CR. This may be related to the negative charge of the GO + itself in pH 6.5 solution. The negatively charged material surface would adsorb more RhB and MB molecules, so more photogenerated holes can contact RhB and MB molecules to participate in the degradation process, thus inhibiting the recombination of photogenerated holes and electrons.

3.8. Electrical Property and Stability.
Zeta potential is a measure of the strength of mutual repulsion or attraction between particles. The zeta potential results of the GO + are shown in Figure 13. When pH is less than 4.5 and pH is greater than 6.5, the surface of the GO+ is negatively charged. At this time, there is repulsion between catalytic materials, resulting in the steric effect of catalytic material particles, indicating that the GO + has strong stability. In

practical application, the reusability of photocatalyst is particularly important [36]. The activity of the photocatalytic material had not changed significantly after 5 times of recycling (Figure 14), and the degradation rate of RhB was still more than 90.0%, indicating that the GO + has good photocatalytic stability and reusability. As a visible light catalyst, it has great potential in practical production.

3.9. Free Radical Detection and Capture Test.
In order to intuitively understand the generation of O_2^- and OH during light irradiation of the GO+, the active substances under visible light irradiation were determined by ESR technology with deionized water as solvent. With deionized water as solvent, the active substances under visible light irradiation were determined by ESR technology. As shown in Figure 15, the signals of DMPO-OH and DMPO-O_2^- were not detected
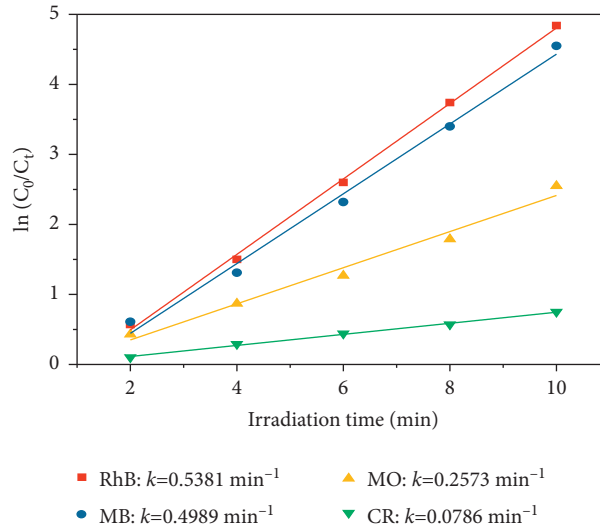
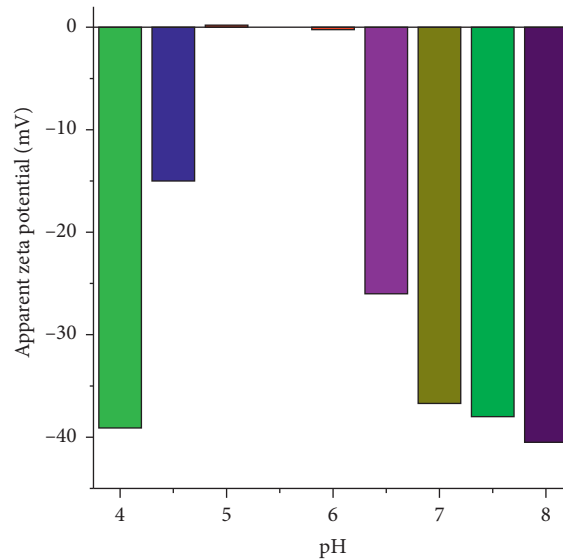FIGURE 12: The first-order kinetics rate constant of photodegradation.

FIGURE 13: Potential distribution.

in dark conditions. However, the characteristic quadruple peaks of DMPO-O_2^- and DMPO-OH could be clearly observed after 5 and 10 min of visible light ($\lambda > 420$ nm). Figure 15(a) shows that the signal peak intensity ratio is about 1 : 1:1 : 1, with the hyperfine splitting constant values: $\alpha_N = 1.319$ mT, $\alpha_H^\beta = 1.038$ mT, and $g = 2.00073$. Therefore, it can be judged that the peak is the characteristic signal peak of the DMPO-O_2^- [37]. Figure 15(b) shows that the peak intensity ratio of spectral signal is 1 : 2:2 : 1, with the hyperfine splitting constant values: $\alpha_N = \alpha_H^\beta = 1.500$ mT, $g = 2.00087$, which is an important sign for ESR technology to distinguish -OH [38]. With the increase in irradiation time, the peaks intensity of DMPO-OH and DMPO-O_2^- increased gradually. The results show that OH and O_2^- appear under light conditions, and light irradiation is a necessary condition to stimulate active substances.

In order to better understand the active substances that play a major role in the photocatalytic degradation of RhB by the GO+, the free radical quench experiments were carried out. Tert butyl alcohol (TBA, 5 mL), disodium EDTA (EDTA-2Na, 0.2 g), and p-benzoquinone (p-BQ, 0.2 g) were used as scavengers for ·OH, h+, and ·O_2^-, respectively.

Figure 16 shows the photocatalytic degradation rate and fitting kinetics of RhB with and without different scavengers. With no scavenger, the degradation rate of RhB in 12 min is 99%, and the k is 0.3069 min^{-1}. As a ·O_2^- scavenger, the addition of p-BQ greatly reduced the degradation rate, and only 9.23% of RhB was degraded, which signifies that a large amount of ·O_2^- was produced, and ·$O2^-$ was a main reactive active species. The addition of EDTA-2Na greatly delayed the degradation process, with the k
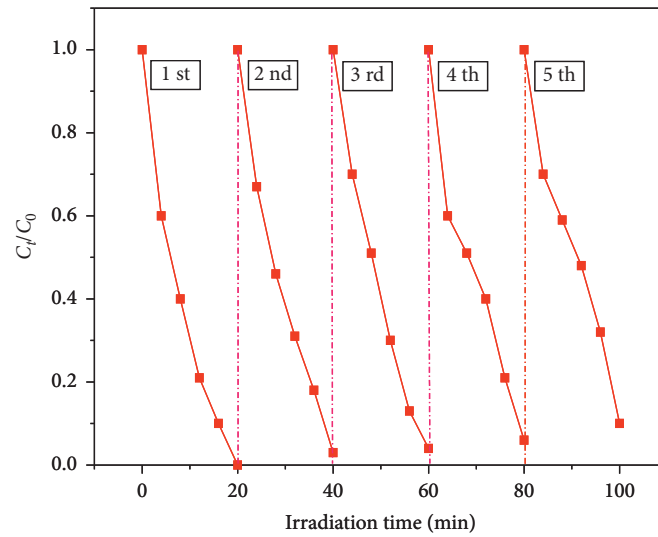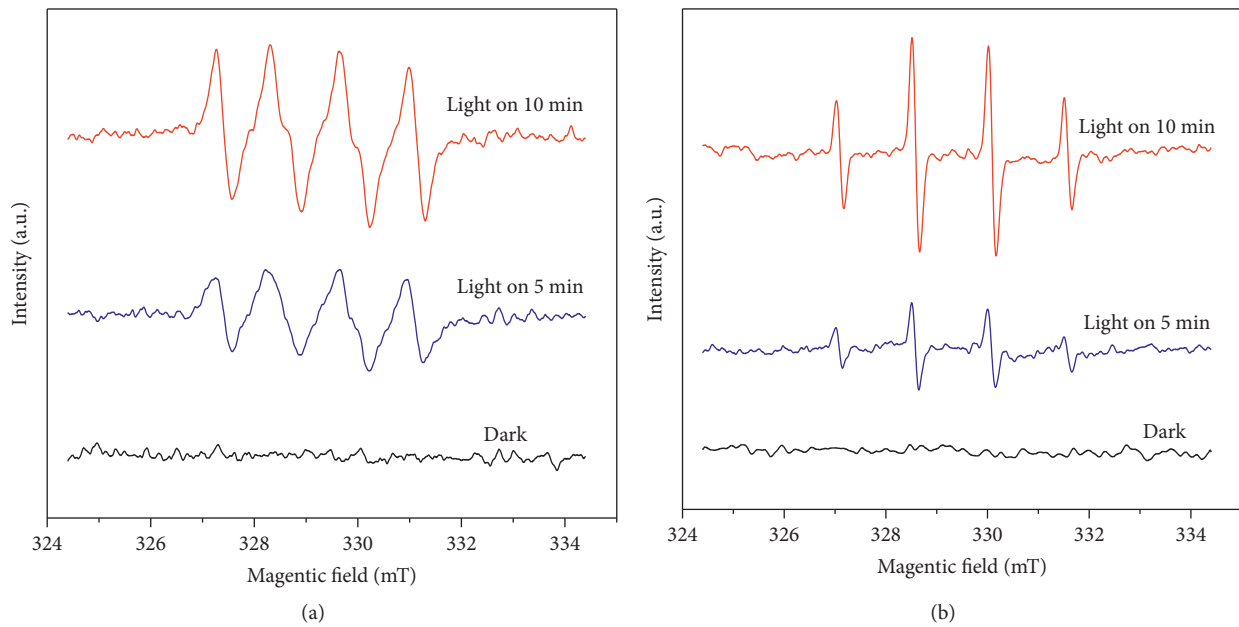
FIGURE 14: Stability test of GO+.

(a)

(b)

FIGURE 15: ESR spectra of superoxide radical and hydroxyl radical: (a)$\cdot O_2^-$, (b)$\cdot OH$.

about $0.1267\,min^{-1}$, which means that h^+ was also a main reactive active species. The addition of TBA had little effect on photocatalytic degradation, indicating that $\cdot OH$ was not the main active substance. The above results show that in the photocatalytic degradation of RhB, $\cdot O_2^-$ plays a leading role, followed by h^+, while $\cdot OH$ does not play a major role [39].

3.10. Photocatalytic Mechanism Analysis. Under visible light irradiation, Ag nanoparticles (AgNPs) on the surface of the GO+ were excited by the SPR to form electron-hole pairs (Figure 17) [40]. Because the Fermi level of AgNPs is relatively low compared with the conduction band phase of AgCl, and the existence of Cl^- on the surface of AgCl makes the surface of AgCl negatively charged, resulting in a polarization effect, the generated e^- quickly moved from AgCl to the surface of AgNPs. Because the conduction band edge potential ($-0.75\,eV$) formed by the antibond π^* orbit of GO is lower than that of hydrogen ($-0.046\,eV$), GO can be used as the acceptor of photoexcited electrons due to its small band gap width [41], so that the electrons on the surface of AgNPs could be quickly transferred to the GO surface, and then captured by O_2 in the solution to form $\cdot O_2$ -, and then decompose RhB, realizing the effective separation of photogenerated electron-hole pairs [42]. In the meantime, the photogenerated h^+ was transferred to the AgCl surface. The h^+ itself had strong oxidation and could effectively remove pollutants. The h^+ of AgCl surface could also interact with Cl^- to form Cl^0. Cl^0 had strong oxidation ability to oxidize
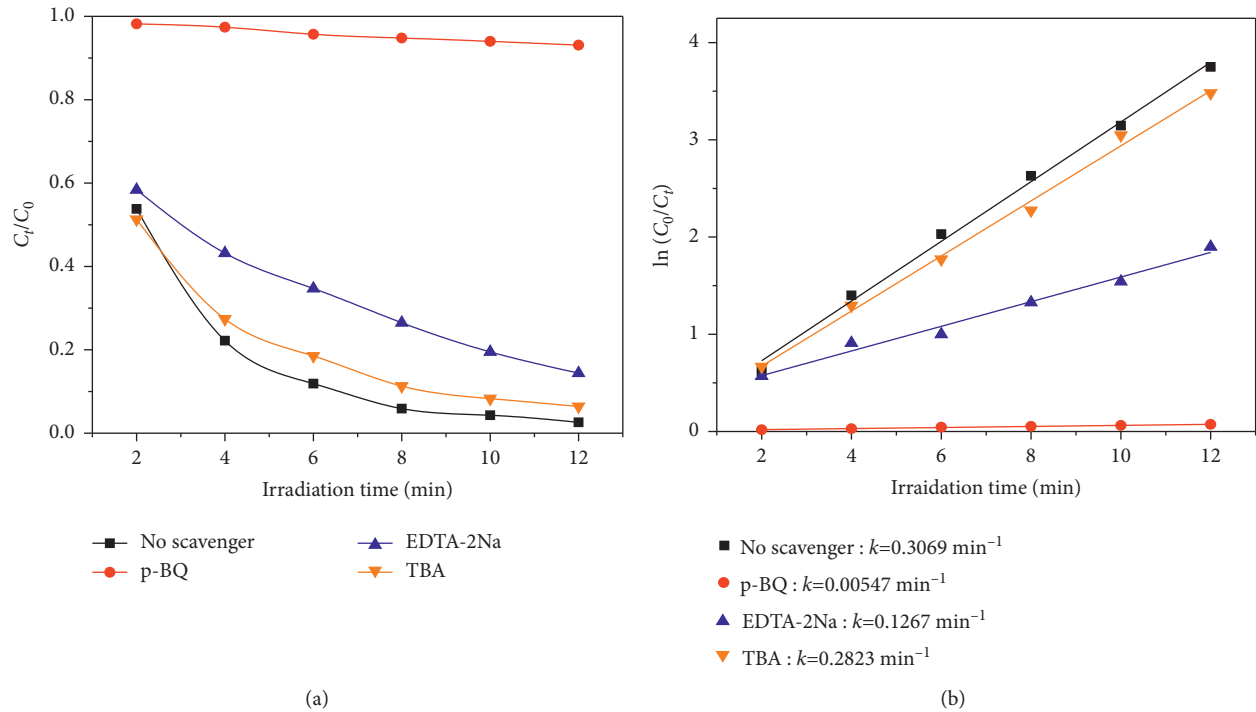
FIGURE 16: (a) Degradation rate of RhB with different scavengers by the GO+, and (b) the k of photodegradation.
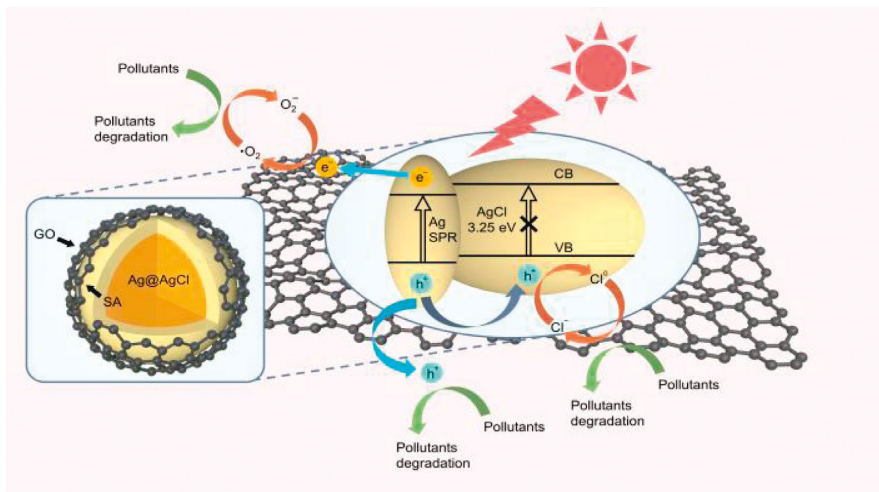

FIGURE 17: Reaction mechanism of degradation by the GO + under visible light irradiation.

the organic molecules adsorbed on the catalyst surface. Meanwhile, Cl^0 was reduced to Cl^-, which effectively ensured the stability of the catalytic system [1]. The addition of GO in GO + material could effectively capture e^- on the surface of AgNPs, inhibit the recombination of photogenerated electrons and holes, and improve the charge separation efficiency and the photocatalytic performance of the composites.

4. Conclusion

The GO + prepared by chemical coupling, in-situ deposition, and photoreduction has the advantages of simple preparation, high loading rate, response to both UV and visible light, especially the wide absorption band under visible light. Large specific surface area is conducive to adsorb more dye molecules and effectively improve the visible light catalytic activity.

The GO + has good degradation effect on RhB, MB, MO, and other simulated dye wastewater, with high catalytic efficiency and short catalytic time. Their degradation processes were in line with the quasi-first-order reaction kinetics. Holes (h^+) and superoxide radical ($\cdot O_2^-$) were the main active species for the degradation of RhB.

The catalytic material is small granular, has good photocatalytic stability and reusability, and is easy to recycle. As

a visible light catalyst, it has great potential in practical production.

Data Availability

The experimental data used to support the findings of this study are available from the corresponding author upon request.

Conflicts of Interest

The authors declare that they have no conflicts of interest to report regarding the present study.

References

[1] P. Wang, B. B. Huang, X. Y. Qin et al., "Ag@AgCl:a highly efficient and stable photocatalyst active under visible light," *Angewandte Chemie International Edition*, vol. 47, no. 41, pp. 7931–7933, 2008.

[2] C. H. An, S. Peng, and Y. G. Sun, "Facile synthesis of sunlight-driven AgCl:Ag plasmonic nanophotocatalyst," *Advanced Materials*, vol. 22, no. 23, pp. 2570–2574, 2010.

[3] Y. P. Bi and J. H. Ye, "In situ oxidation synthesis of Ag/AgCl core–shell nanowires and their photocatalytic properties," *Chemical Communications*, vol. 43, pp. 6551–6553, 2009.

[4] X. L. Ma, Y. X. Tang, H. J. Tao et al., "Uniform spatial distribution of a nanostructured Ag/AgCl plasmonic photocatalyst and its segregative membrane towards visible light-driven photodegradation," *CrystEngComm*, vol. 18, no. 20, pp. 3725–3733, 2016.

[5] J. Low, S. Qiu, D. Xu, C. Jiang, and B. Cheng, "Direct evidence and enhancement of surface plasmon resonance effect on Ag-loaded TiO2 nanotube arrays for photocatalytic CO_2 reduction," *Applied Surface Science*, vol. 434, no. Mar.15, pp. 423–432, 2018.

[6] M. Zhao, Q. Yuan, H. Zhang, C. Li, Y. Wang, and W. Wang, "Synergy of adsorption and photocatalysis on removal of high-concentration dye by Ag/AgCl/$Bi_6O_4(OH)_4(NO_3)_6 \bullet H_2O$ nanocomposite using $Bi_{12}O_{17}Cl_2$ as bismuth source," *Journal of Alloys and Compounds*, vol. 782, pp. 1049–1057, 2019.

[7] L. L. Sun, C. Y. Liu, J. Z. Li et al., "Fast electron transfer and enhanced visible light photocatalytic activity by using poly-o-phenylenediamine modified AgCl/g-C_3N_4 nanosheets," *Chinese Journal of Catalysis*, vol. 40, no. 1, pp. 80–94, 2019.

[8] S. Asadzadeh-Khaneghah, A. Habibiyangjeh, and M. Abedi, "Decoration of carbon dots and AgCl over g-C3N4 nanosheets: novel photocatalysts with substantially improved activity under visible light," *Separation and Purification Technology*, vol. 199, pp. 64–77, 2018.

[9] J. Q. Xiao, K. S. Lin, and Y. Yu, "Novel Ag@AgCl@AgBr heterostructured nanotubes as high-performance visible-light photocatalysts for decomposition of dyes," *Catalysis Today*, vol. 314, pp. 10–19, 2018.

[10] X. G. Kong, L. Li, Z. L. Guo et al., "Soft chemical in situ synthesis and photocatalytic performance of 1D Ag/AgCl/V_2O_5 hetero-nanostructures," *Materials Letters*, vol. 183, no. 15, pp. 215–218, 2016.

[11] A. Ou, J. Luo, and H. Cao, "Preparation of Ag@AgCl modified $Bi_4Ti_3O_{12}$ and its visible light catalytic performance," *Acta Materiae Compositae Sinica*, vol. 39, no. 4, pp. 1648–1656, 2022, (in Chinese).

[12] Q. Ke, H. Chang, and B. Huang, "Preparation and photocatalytic performance of Ag/AgCl/MoO_3 compositess," *Journal of Materials Science & Engineering*, vol. 38, no. 02, pp. 238–244, 2020.

[13] W. B. Wu, J. Wang, T. Y. Zhang et al., "Controllable synthesis of Ag/AgCl@MIL-88A *via in situ* growth method for morphology-dependent photocatalytic performance," *Journal of Materials Chemistry C*, vol. 7, no. 18, pp. 5451–5460, 2019.

[14] H. A. Ghaly, A. S. El-Kalliny, T. A. Gad-Allah, N. E. A. A. El-Sattar, and E. R. Souaya, "Stable plasmonic Ag/AgCl-polyaniline photoactive composite for degradation of organic contaminants under solar light," *RSC Advances*, vol. 21, pp. 12726–12736, 2017.

[15] Y. G. Xu, H. Xu, H. Li, J. Xia, C. Liu, and L. Liu, "Enhanced photocatalytic activity of new photocatalyst Ag/AgCl/ZnO," *Journal of Alloys and Compounds*, vol. 509, no. 7, pp. 3286–3292, 2011.

[16] A. Molea, V. Popescu, N. A. Rowson, and A. M. Dinescu, "Influence of pH on the formulation of TiO_2 nano-crystalline powders with high photocatalytic activity," *Powder Technology*, no. 253, pp. 22–28, 2014.

[17] M. C. Long, Y. L. Qin, C. Chen, X. Guo, B. Tan, and W. Cai, "Origin of visible light photoactivity of reduced graphene oxide/TiO2 by in situhydrothermal growth of undergrown TiO_2 with graphene oxide," *Journal of Physical Chemistry C*, vol. 117, no. 32, pp. 16734–16741, 2013.

[18] G. D. Chen, M. Sun, Q. Wei, Y. Zhang, B. Zhu, and B. Du, "Ag_3PO_4/graphene-oxide composite with remarkably enhanced visible-light-driven photocatalytic activity toward dyes in water," *Journal of Hazardous Materials*, vol. 244-245, pp. 86–93, 2013.

[19] Z. L. Xiu, Z. Wu, X. P. Hao, et al.,Q. Lu, and S. Liu, "Graphene oxide wrapped Ag_3PO_4 sub-microparticles with highly enhanced photocatalytic activity and stability under visible light irra-diation," *Materials Research Bulletin*, vol. 59, pp. 192–198, 2014.

[20] S. Qu, Y. Xiong, and J. Zhang, "Fabrication of GO/CDots/BiOI nanocomposites with enhanced photocat- alytic 4-chlorophenol degradation and mechanism in-Sight," *Separation and Purification Technology*, vol. 210, pp. 382–389, 2019.

[21] S. Xu, T. Zhu, and Y. Qiao, "Fabrication of Z-scheme BiVO4/GO/g-C3N4 photocatalyst with efficient visble-light photocatalytic performance," *Journal of Inorganic Materials*, vol. 35, no. 07, pp. 839–846, 2020.

[22] D. A. Giannakoudakis, J. A. Arcibar-Orozco, and T. J. Bandosz, "Effect of GO phase in Zn(OH) (2)/GO composite on the extent of photocatalytic reactive adsorption of mustard gas surrogate," *Applied Catalysis B: Environmental*, vol. 183, pp. 37–46, 2016.

[23] Y. Gao, Y. Li, L. Zhang et al., "Adsorption and removal of tetracycline antibiotics from aqueous solution by graphene oxide," *Journal of Colloid and Interface Science*, vol. 368, no. 1, pp. 540–546, 2012.

[24] C. Xu, Y. Yuan, A. Cui, and R. Yuan, "In situ controllable synthesis of Ag@AgCl core–shell nanoparticles on graphene oxide sheets," *Journal of Materials Science*, vol. 48, no. 2, pp. 967–973, 2013.

[25] J. J. Lu, Y. H. Gu, Y. Chen, X. Yan, Y. J. Guo, and W. Z. Lang, "Ultrahigh permeability of graphene-based membranes by adjusting D-spacing with poly (ethylene imine) for the separation of dye wastewater," *Separation and Purification Technology*, vol. 210, pp. 737–745, 2019.

[26] A. Kurniawan, S. Muneekaew, C. W. Hung, S. H. Chou, and M. J. Wang, "Modulated transdermal delivery of nonsteroidal anti-inflammatory drug by macroporous poly(vinyl alcohol)-graphene oxide nanocomposite films (vinyl alcohol)-graphene oxide nanocomposite films," *International Journal of Pharmaceutics*, vol. 566, pp. 708–716, 2019.

[27] P. He, J. Zhou, H. Tang et al., "Electrochemically modified graphite for fast preparation of large-sized graphene oxide," *Journal of Colloid and Interface Science*, vol. 542, pp. 387–391, 2019.

[28] S. C. Zhang, P. Liu, J. Xu, and X. S. Zhao, "Preparation of poly(vinyl alcohol)-grafted graphene oxide/poly(vinyl alcohol) nanocomposites via in-situ low-temperature emulsion polymerization and their thermal and mechanical characterization(vinyl alcohol)-grafted graphene oxide/poly(vinyl alcohol)nanocomposites via in situ low-temperature emulsion polymerization and their thermal and mechanical characterization," *Applied Surface Science*, vol. 396, pp. 1098–1107, 2017.

[29] X. Zhang, Q. Li, W. Han et al., "Raman identification of edge alignment of bilayer graphene down to the nanometer scale," *Nanoscale*, vol. 6, no. 13, pp. 7519–7525, 2014.

[30] K. N. Kudin, B. Ozbas, H. C. Schniepp, R. K. Prud'homme, I. A. Aksay, and R. Car, "Raman spectra of graphite oxide and functionalized graphene sheets," *Nano Letters*, vol. 8, no. 1, pp. 36–41, 2008.

[31] A. K. Das, R. K. Layek, N. H. Kim, D. Jung, and J. H. Lee, "Reduced graphene oxide (RGO)-supported NiC-$o_2O_4$nanoparticles: an electrocatalyst for methanol oxidation," *Nanoscale*, vol. 6, no. 18, pp. 10657–10665, 2014.

[32] M. R. Vengatesan, S. Singh, S. Stephen, K. Prasanna, C. Lee, and V. Mittal, "Facile synthesis of thermally reduced graphene oxide-sepiolite nanohybrid via intercalation and thermal reduction method," *Applied Clay Science*, vol. 135, pp. 510–515, 2017.

[33] A. L. Boreen, W. A. Arnold, and K. McNeill, "Photochemical fate of sulfa drugs in the aquatic environment: sulfadrugs containing five-membered heterocyclic groups," *Environmental Science & Technology*, vol. 38, no. 14, pp. 3933–3940, 2004.

[34] Y. Yang, Y. Zhang, M. Dong, T. Yan, M. Zhang, and Q. Zeng, "Highly efficient degradation of thidiazuron with Ag/AgCl-activated carbon composites under LED light irradiation," *Journal of Hazardous Materials*, vol. 335, pp. 92–99, 2017.

[35] Z. Geng, Z. Chen, Z. Li et al., "Enhanced photocatalytic conversion and selectivity of nitrate reduction to nitrogen over AgCl/TiO_2 nanotubes," *Dalton Transactions*, vol. 47, no. 32, pp. 11104–11112, 2018.

[36] H. Y. Mou, C. X. Song, Y. H. Zhou, B. Zhang, and D. Wang, "Design and synthesis of porous Ag/ZnO nanosheets assemblies as super photocatalysts for enhanced visible-light degradation of 4-nitrophenol and hydrogen evolution," *Applied Catalysis B: Environmental*, vol. 221, pp. 565–573, 2018.

[37] V. Brezo and A. Stasko, "Spin trap study of hydroxyl radicals formed in the photocatalytic systerm TO_2-water-*p*-cresol-oxygen [J]," *Journal of Catalysis*, vol. 14, no. 1, pp. 156–162, 1994.

[38] A. V. Taborda, M. A. Brusa, and M. A. Grela, "Photocatalytic degradation of phthalic acid on TiO_2 nanoparticles," *Applied Catalysis, A: General*, vol. 208, no. 1-2, pp. 419–426, 2001.

[39] Y. Wang, M. Y. Wu, and W. Y. Lei, "Preparation of graphene oxide load Ag3PO4@PANI composite and its photocatalytic performance," vol. 39, 2022 (in Chinese).

[40] Q. Zhu, W. S. Wang, L. Lin et al., "Facile synthesis of the novel Ag_3VO_4/AgBr/Ag plasmonic photocatalyst with enhanced photocatalytic activity and stability," *Journal of Physical Chemistry C*, vol. 117, no. 11, pp. 5894–5900, 2013.

[41] A. S. Kumbhar, M. K. Kinnan, and G. Chumanov, "Multipole plasmon resonances of submicron silver particles," *Journal of the American Chemical Society*, vol. 127, no. 36, pp. 12444-12445, 2005.

[42] B. Cai, J. Wang, S. Gan, D. Han, Z. Wu, and L. Niu, "A distinctive red Ag/AgCl photocatalyst with efficient photocatalytic oxidative and reductive activities," *Journal of Materials Chemistry*, vol. 2, no. 15, pp. 5280–5286, 2014.